Control of Magnetization-Reversal Mechanism via Uniaxial Anisotropy Strength in $La_{0.67}Sr_{0.33}MnO_3$ Electrodes for Spintronic Devices

L. C. Phillips,[1,2,*] W. Yan,[1] X. Moya,[1,3] M. Ghidini,[1,4] F. Maccherozzi,[5] S. S. Dhesi,[5] and N. D. Mathur[1,†]
[1]*Department of Materials Science, University of Cambridge, Cambridge CB3 0FS, United Kingdom*
[2]*Unité Mixte de Physique CNRS/Thales, 1 avenue Augustin Fresnel, 91767 Palaiseau, France*
[3]*Facultat de Física, Departament d'Estructura i Constituents de la Matèria, Universitat de Barcelona,*
Martí i Franquès 1, E-08028 Barcelona, Catalonia, Spain
[4]*DiFeST, University of Parma, viale G. P. Usberti 7/A, 43124 Parma, Italy*
[5]*Diamond Light Source, Chilton, Didcot, Oxfordshire OX11 0DE, United Kingdom*

(Received 10 March 2015; revised manuscript received 22 September 2015; published 14 December 2015)

Spintronic device performance depends critically on magnetization reversal mechanisms, but these are rarely imaged in order to verify correct operation. Here we use magnetometry and magnetic imaging to study thin films and patterned elements of highly spin-polarized $La_{0.67}Sr_{0.33}MnO_3$ grown epitaxially on $NdGaO_3$ substrates whose crystallographic orientation determines magnetic anisotropy strength. Small anisotropy yields gradual magnetization reversal via nucleation and propagation of small-needle domains, whereas large anisotropy yields a single nucleation event resulting in sharp and complete magnetization reversal. We explain these observed differences using micromagnetic simulations, and exploit them in order to quantify the effect of $La_{0.67}Sr_{0.33}MnO_3$ electrode behavior on spin signals from hypothetical devices. Our work, therefore, highlights the dramatic discrepancies that can arise between the design and performance of spintronic devices.

DOI: 10.1103/PhysRevApplied.4.064004

I. INTRODUCTION

Spintronic devices represent key building blocks in future circuits designed to perform reconfigurable digital logic and binary information storage. These devices exploit the flow of spin-polarized electrical currents that are typically generated inside electrodes made from ferromagnetic metals or ferromagnetic metallic oxides [1]. The archetypal spintronic device displays two states of electrical resistance that are associated with parallel (P) and antiparallel (AP) configurations of two magnetic electrodes separated by a nonmagnetic material, namely, a conducting channel (spin valve) or an ultrathin insulating barrier (magnetic tunnel junction). To interconvert between fully P and AP states requires complete magnetization reversal, most usefully in a repeatable manner with sharp switching. In principle, one can employ nanoscale patterned elements in which single magnetic domains switch sharply by coherent rotation or curling [2,3]. However, existing devices are fabricated on longer length scales such that magnetization reversal is prone to proceed in a gradual manner via domain nucleation and growth [4]. As a result, existing spin-valve prototypes are liable to exhibit gradual changes of resistance associated with complex magnetic domain configurations in which fully P and AP states are likely not developed [5,6]. This gradual switching is desirable for spintronic devices such as magnetic-field sensors, memristors, or artificial neurons [7,8] but not spin valves. There is, thus, a pressing need to understand the rarely studied phenomenon of magnetization reversal in patterned electrodes.

Ideally, spintronic studies should include experimental observations of electrode magnetization reversal, which cannot be reliably inferred from the literature on unpatterned films or patterned elements [9–11] because of great sensitivity to composition, size, shape, and microstructure. Here we study magnetization reversal in highly spin-polarized [12] $La_{0.67}Sr_{0.33}MnO_3$ (LSMO) by fabricating epitaxial thin films, patterned elements, and, ultimately, spintronic electrodes. We choose this material because it is commonly employed in testbed electrodes, e.g., for vertical spin transport through oxide tunnel barriers [13,14] and organic layers [15] and for lateral spin transport through carbon nanotubes [16]. Magnetization reversal in LSMO electrodes has not been investigated, and just as for other materials, it cannot be inferred from micromagnetic studies of unpatterned films [17–23] or patterned elements [24–26]. This hole in the literature is surprising given the extensive work on LSMO during the last two decades.

Our strategy is to exploit the response of LSMO films to epitaxial strain [27–30] in order to tailor the strength of the uniaxial in-plane magnetic anisotropy that arises in films grown on $NdGaO_3$ (NGO) substrates in two crystallographic orientations. We image patterned LSMO elements and electrodes using photoelectron emission microscopy

---

[*] lee.phillips@cantab.net
[†] ndm12@cam.ac.uk

(PEEM) with magnetic contrast from x-ray magnetic circular dichroism (XMCD). Films with small anisotropy exhibit gradual magnetization reversal via nucleation and propagation of small-needle domains, i.e., "memristive" switching compatible with multiple resistance levels in spintronic memristors [7,8]. Films with large anisotropy exhibit sharp and complete magnetization reversal following a single nucleation event, i.e., binary switching. This result is valid down to our smallest feature, approximately 2 μm wide. We subsequently employ micromagnetic simulations, first to investigate the structure and energetics of a single domain wall (DW) in each type of film and then to confirm that the strength of the uniaxial in-plane magnetic anisotropy determines whether one observes gradual reversal processes limited by DW propagation or sharp reversal processes limited by domain nucleation. Finally, to show how imaging is essential in order to avoid discrepancies between the design and performance of spintronic devices, we demonstrate the dramatic effect of gradual switching on the performance of hypothetical devices by using a parallel resistor model to describe LSMO electrodes connected by nonmagnetic materials with no spin relaxation, i.e., "perfect" channels.

II. EXPERIMENT DETAILS

A. Film deposition

Epitaxial LSMO films are grown by pulsed-laser deposition (KrF excimer laser, $\lambda = 248$ nm) at 1 Hz with laser fluence 2 $\mathrm{J\,cm^{-2}}$ and spot size (8 ± 1) $\mathrm{mm^2}$, in 15 Pa of oxygen onto untwinned single-crystal $\mathrm{NdGaO_3}$ substrates (Crystal GmbH) that are preheated to 775 °C. The target-substrate distance is 8 cm, and the deposition rate is (0.41 ± 0.03) $\mathrm{Å\,pulse^{-1}}$. Samples are postannealed in 0.5-bar $\mathrm{O_2}$ at 700 °C or 750 °C for 1 h. We observe no appreciable change in structural or magnetic properties as a function of film thickness, i.e., 26 nm [Fig. 1(a)], 22 nm [Fig. 1(b)], 57 nm [Fig. 2(a)], 32 nm [Fig. 2(b)], 67 nm [Figs. 3(a) and 3(b)], 53 nm [Fig. 3(c)], 61 nm [Fig. 3(d)], 60 nm [Figs. 4(a) and 4(b)], and 60 nm [Fig. 4(d)].

B. Film characterization

Films are characterized by atomic force microscopy using a Digital Instruments Nanoscope III and by x-ray diffraction (XRD) using a Philips X'Pert GEN 6 high-resolution diffractometer. All films show atomically flat terraces, and there is a low density < 1 $\mu\mathrm{m}^{-2}$ of small particles with heights < 20 nm. XRD θ-2θ scans show coherent strain with Laue fringes in all samples.

C. Magnetometry

We use a Princeton MicroMag 3900 vibrating sample magnetometer with gas-flow cryostat. The paramagnetism of the NGO substrate is corrected via a linear fit to the high-field response such that $\mathrm{d}M/\mathrm{d}H = 0$. Vertical offsets are corrected by centering.

D. Pattern definition

Electrodes and dots are defined by UV photolithography and $\mathrm{Ar^+}$-ion milling with 0.5-keV ions at (4 ± 1) $\mathrm{nm\,min^{-1}}$ to a depth of over 100 nm. To avoid charging in PEEM, we evaporate approximately 50 nm of Au onto milled regions prior to lift-off in order to ensure a conducting sample surface. The proximity effect of Au on LSMO [31] extends only approximately 4 nm into the film and may be neglected.

E. XMCD-PEEM imaging

XMCD-PEEM measurements at approximately 150 K are performed at Diamond Light Source beam line I06 with the x-ray beam at a grazing incidence angle of 16°, using an Elmitec SPELEEM III microscope to image the local zero-field magnetization to a probe depth of approximately 7 nm and a typical lateral resolution of approximately 50 nm. After imaging with right (+) and left (−) circularly polarized light, we calculate x-ray absorption spectroscopy (XAS) $(I^+ + I^-)$ and XMCD asymmetry $(I^+ - I^-)/(I^+ + I^-)$ for each pixel, where the influence of inhomogeneous illumination is avoided by evaluating $I^\pm = (I^\pm_{\mathrm{on}} - I^\pm_{\mathrm{off}})/I^\pm_{\mathrm{off}}$, which is the relative intensity of secondary-electron emission arising from x-ray absorption on ($I^\pm_{\mathrm{on}}$ at 639.5 eV) and off ($I^\pm_{\mathrm{off}}$ at 630 eV) the Mn L_3 edge. Images for each x-ray energy and beam polarization are acquired during 10-s exposure times. With the exception of Figs. 3(b) and 4(d), each XMCD-PEEM image that we present is constructed via an averaging process based on two [Figs. 3(c) and 3(d)] or three [Figs. 4(a) and 4(b)] such images, which are available at [32]. Pulses of magnetic field are applied along the in-plane easy axis, between measurements at magnetic remanence, via a coil on the sample cartridge.

III. COMPUTATIONAL DETAILS

A. LSMO exchange stiffness

Exchange stiffness $A = JS^2/a = 2.1 \times 10^{-12}$ $\mathrm{J\,m^{-1}}$ is calculated from lattice constant $a = 3.88$ Å, spin $S = 1.83$ representing a weighted average of $S = 2$ ($\mathrm{Mn^{3+}}$) and $S = 3/2$ ($\mathrm{Mn^{4+}}$), and Heisenberg exchange energy [33] $J = 3k_B T_C/2zS(S+1)$ with $z = 6$ nearest neighbors, Curie temperature $T_C = 370$ K, and Boltzmann constant k_B. We do not subject A to finite-temperature renormalization [34] because the film magnetization varies little below our 150-K measurement temperature.

B. Micromagnetic simulations

We use the OOMMF micromagnetic package [35] to simulate isolated LSMO slabs that represent patterned epitaxial films. The paramagnetic NGO substrates may be neglected. Values for magnetic anisotropy constants [Eq. (1)] are listed in Table I. We represent K_a by a negative uniaxial anisotropy along the in-plane hard axis and K_c by a positive uniaxial anisotropy along the out-of-plane direction. All simulations assume local moments that correspond to

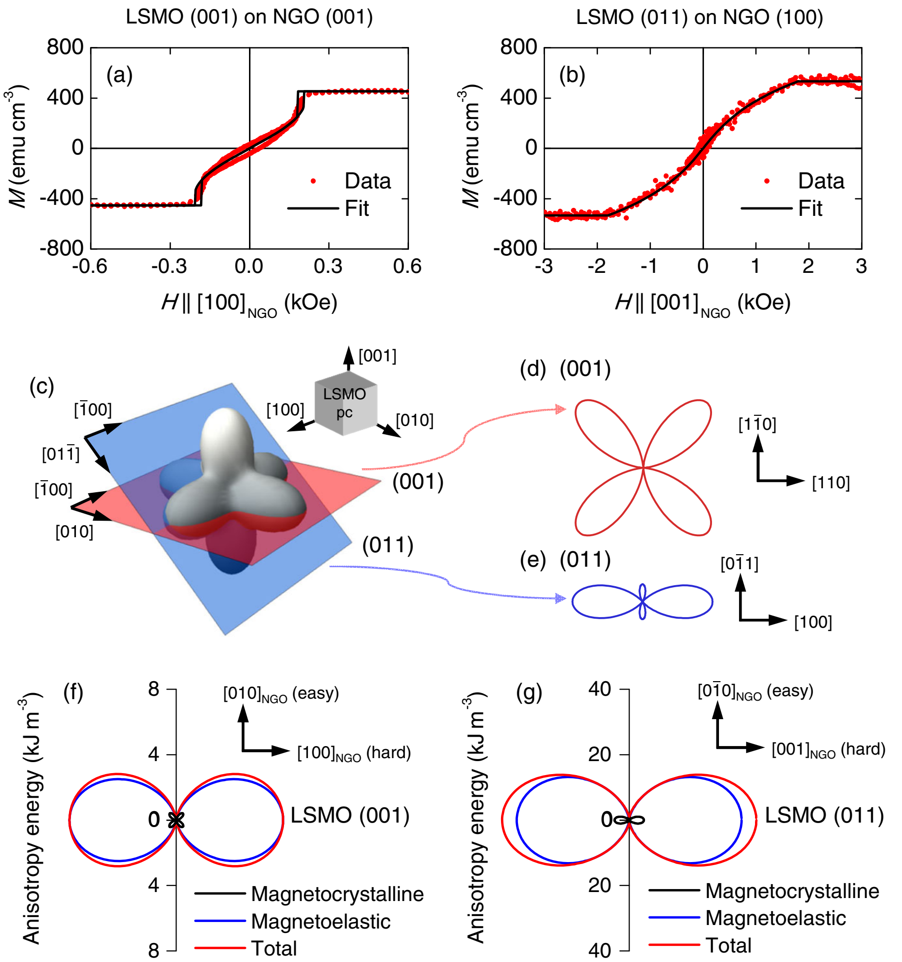

FIG. 1. Anisotropy of LSMO films at 150 K. Measurements of in-plane hard-axis magnetization M versus field H, for (a) LSMO (001) on NGO (001) and (b) LSMO (011) on NGO (100). (c) 3D polar plot of negative cubic anisotropy on an arbitrary scale, intercepted by (001) and (011) planes of LSMO passing through the origin. Inset: schematic showing the pc axes of LSMO. 2D polar plots of negative cubic anisotropy on an arbitrary scale projected onto (d) (001) and (e) (011) planes of LSMO. Fits to the data in (a),(b) yield anisotropy energy constants (Table I) that are used to construct (f),(g) 2D polar plots.

saturation magnetization $M_s = 460\ \mathrm{kA\,m^{-1}}$, exchange stiffness $A = 2.1 \times 10^{-12}\ \mathrm{J\,m^{-1}}$, and a 4-nm mesh that is comparable with exchange length $\sqrt{2A/\mu_0 M_s^2} = 4.0$ nm. For DW energy simulations (Fig. 5), we use the OOMMF energy solver to iteratively find a minimum using the conjugate-gradient method. The criterion for convergence is $|\mathbf{m} \times \mathbf{H}_{\mathrm{tot}} \times \mathbf{m}| < 0.1\ \mathrm{A\,m^{-1}}$, for each moment $\mathbf{m}$ that experiences total field $\mathbf{H}_{\mathrm{tot}}$. DW line energy per unit length is calculated by first evaluating $[E_{\mathrm{tot}}(L_0 + \Delta L) - E_{\mathrm{tot}}(L_0)]/\Delta L$, where $E_{\mathrm{tot}}(L)$ is the total energy for an easy-axis line of length L, and then subtracting the corresponding expression for a separate simulation with no DW (not shown). Here, $L_0 = 2000$ nm and $\Delta L = 4$ nm corresponds to the mesh spacing. For simulations of magnetization reversal using the energy solver, we allow 100 iterations between 1-Oe field steps.

IV. RESULTS AND DISCUSSION

A. Structural data and magnetometry

LSMO films indexed as pseudocubic (pc) are grown in the (001) and (011) orientations on, respectively, the (001) and (100) surfaces of NGO substrates indexed as orthorhombic (see Sec. II). Both LSMO (001) on NGO (001) and LSMO (011) on NGO (100) experience similar in-plane distortions, with compressive strain along one principal axis and tensile strain along the other [−1.11% and +0.16% for LSMO (001) and −0.70% and +0.16% for LSMO (011)] [30]. Our films show coherent strain [36], and strong ferromagnetism with similar values of saturation magnetization M_s in the range 450–500 $\mathrm{emu\,cm^{-3}}$ at our 150-K measurement temperature [Figs. 1(a) and 2(b)]. As expected [30], film magnetization $\mathbf{M}$ lies in plane due to the large demagnetizing factor associated with the out-of-plane direction.

Figures 1(a) and 1(b) show that the in-plane magnetic hard axes lie along $[100]_{\mathrm{NGO}}$ and $[001]_{\mathrm{NGO}}$ for LSMO (001) and LSMO (011), respectively (easy-axis data appear later in Fig. 2). We assume that coherent in-plane rotation [37,38] for these hard-axis directions is governed by two competing anisotropies. First, negative cubic magnetocrystalline anisotropy $K_1 < 0$ [Fig. 1(c)] projects onto the two film planes as shown in Figs. 1(d) and 1(e). Second, stress-induced uniaxial anisotropy K_a renders the in-plane $[010]_{\mathrm{NGO}}$ direction easy for each type of film. The resulting anisotropy energy density is given by

$$E_K = K_1(\alpha^2\beta^2 + \beta^2\gamma^2 + \gamma^2\alpha^2) + K_a(\cos^2\theta), \quad (1)$$

(a) LSMO (001)

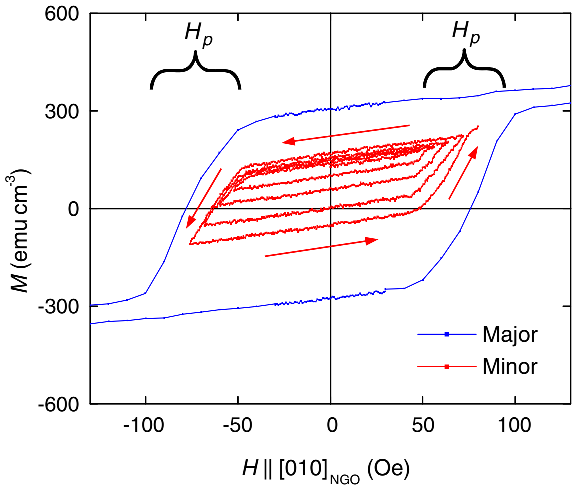

(b) LSMO (011)

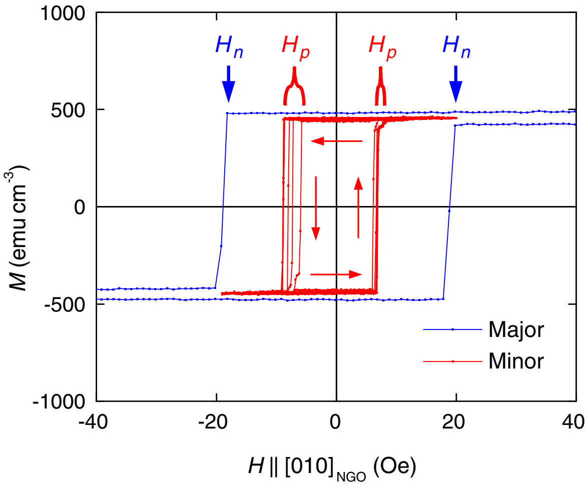

FIG. 2. Easy-axis switching of LSMO films at 150 K. Major (blue) and minor (red) loops of magnetization M versus H, for (a) LSMO (001) and (b) LSMO (011). For minor loops, films are demagnetized to create multiple domains before collecting data in an oscillating field of increasing amplitude. Minor loops grow while cycling in the sense indicated by the red arrows. In (a), values of the resulting propagation field H_p are indicated for both major and minor loops. For the major loop in (b), we identify coercive field H_c^{major} with nucleation field H_n.

where α, β, and γ are the direction cosines of $\mathbf{m}$ with respect to the pseudocubic unit cell of the film, and θ is the angle between $\mathbf{M}$ and the stress-induced in-plane easy axis. Using our previously reported method [where we combine uniaxial and biaxial anisotropy without the generality expressed in Eq. (1)] [29], we fit hard-axis in-plane measurements of magnetization M versus field H [Figs. 1(a) and 1(b)] in order to estimate values of K_1 and K_a (Table I). For both films, the magnetoelastic anisotropy (K_a) dominates the magnetocrystalline anisotropy (K_1) to yield a single easy axis [Figs. 1(f) and 1(g)]. However, the value of K_a for LSMO (011) is around 5 times larger than the corresponding value for LSMO (001), even though the in-plane strains are similar. Therefore, the magnetoelastic response of LSMO is strongly anisotropic, primarily reflecting the effect of asymmetrically distorted MnO_6 octahedra on spin-orbit coupling at the manganese sites [39].

The two different substrate orientations also yield very different easy-axis magnetization reversal characteristics, with gradual switching for LSMO (001) and sharp switching for LSMO (011) (Fig. 2). Major loops (blue traces, Fig. 2) show that the coercive field is lower for LSMO (011) than LSMO (001) even though the former possesses the higher anisotropy. We also present minor loops obtained after demagnetization to achieve a multidomain state (red traces, Fig. 2). This is because minor loops can reveal the coercivity mechanism, e.g., in bulk hard magnets [40]. Here we explore whether the major-loop coercive field H_c^{major} is determined by domain nucleation at nucleation field H_n or the unpinning of preexisting DWs at propagation field H_p. For LSMO (001), the presence of prenucleated domains during minor loops does not reduce the switching field with respect to the major loop, and, therefore, magnetization reversal is not limited by domain nucleation but instead DW pinning [$|H_p| \sim |H_c^{\text{major}}|$, Fig. 2(a)]. For LSMO (011), the presence of prenucleated domains during minor loops reduces the switching field with respect to the major loop, and, therefore, magnetization reversal in the major loop is limited by domain nucleation rather than DW pinning [$|H_p| < |H_c^{\text{major}}|$, Fig. 2(b)]. This absence of DW pinning in LSMO (011) is consistent with the absence of multidomain states in minor loops that are essentially saturated when not switching. By contrast, a wide range of multidomain states can be stabilized in LSMO (001), but the fully saturated state relaxes at remanence even in the major loop [Fig. 2(a)]. The order-of-magnitude discrepancy in propagation field for the two substrate orientations evidences a difference in pinning strengths that can arise intrinsically due to different rhombohedral distortions [41,42] or extrinsically due to microstructural differences that lie beyond our resolution.

B. Magnetization reversal in dots

In order to build on the above investigation of magnetic switching in LSMO films at 150 K, we study large patterned elements at the same temperature. Pulsed easy-axis fields of magnitude H_{pulse} and duration 1 s are applied in order to progressively induce (minor-loop) switching that is monitored between pulses by collecting XMCD-PEEM images at magnetic remanence. First, we study well-separated and, therefore, noninteracting dots, then we study electrodes whose putative spintronic device performance is investigated later in this paper. In both cases, we see that our microscopic observations are consistent with our macroscopic data for unpatterned films (Fig. 2). Our study of remanent states is desirable in the context of achieving

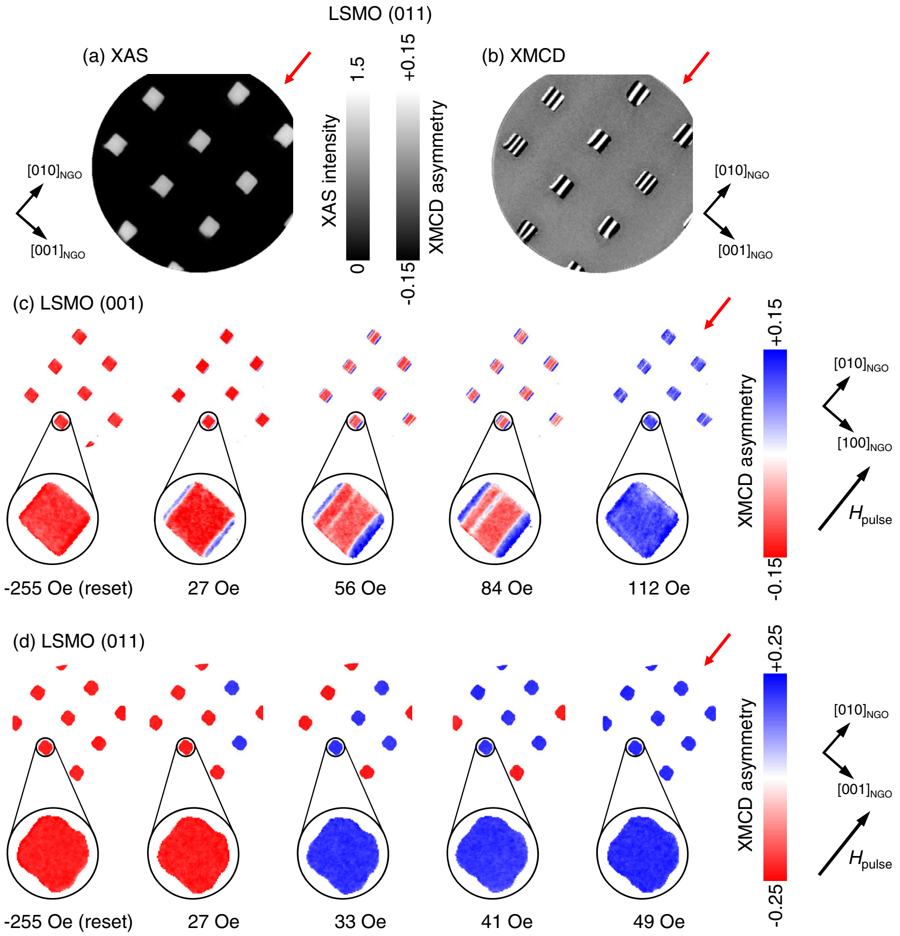

FIG. 3. Visualization of magnetization reversal in square LSMO dots at 150 K. PEEM images of virgin LSMO (011) dots, with (a) chemical contrast from XAS at the Mn L_3 edge and (b) the corresponding magnetic contrast from XMCD. Zero-field XMCD-PEEM images of (c) LSMO (001) dots and (d) LSMO (011) dots after applying easy-axis fields of H_{pulse} as indicated. XMCD asymmetry represents projection of in-plane surface magnetization onto in-plane projection of grazing-incidence beam direction (red arrows). Darkest red contrast depicts magnetization pointing top right; darkest blue contrast depicts magnetization pointing bottom left. All data obtained after zero-field cooling. All dots $5 \times 5\ \mu\mathrm{m}^2$.

nonvolatile P and AP configurations, but the effect of returning from H_{pulse} to remanence is likely to be negligible, as the corresponding minor-loop trajectories are very flat (Fig. 2).

For $5 \times 5\ \mu\mathrm{m}^2$ LSMO (011) dots with a 10-μm nearest-neighbor separation that precludes dipolar coupling [9], PEEM with chemical contrast from XAS confirms dot definition [Fig. 3(a)], and PEEM with magnetic contrast from XMCD confirms an initial arrangement of AP domains [Fig. 3(b)]. For both types of substrates, the initial application of $H_{\mathrm{pulse}} = -255$ Oe saturates the remanent magnetization of each dot [Figs. 3(c) and 3(d)]. For each LSMO (001) dot [Fig. 3(c)], a subsequent increase in positive values of H_{pulse} initially produces remanent states with reverse domains on opposite sides, possibly due to edge relaxation of the large -1.11% compressive strain [30] along $[100]_{\mathrm{NGO}}$. Further processes within each dot ultimately lead to complete magnetization reversal.

For each LSMO (011) dot [Fig. 3(d)], we see no evidence of intermediate states, with magnetization reversal occurring at reproducible fields showing a dot-to-dot variation of 25 Oe $< |H_{\mathrm{pulse}}| <$ 50 Oe, likely due to discrepancies in perimeter roughness. Therefore, adjacent dots patterned from LSMO (011) can adopt the P and AP configuration at remanence, consistent with the square loop of Fig. 2(b). By contrast, the P and AP configuration appears to be inaccessible for LSMO (001) dots, consistent with the sheared loop of Fig. 2(a).

We make two notes regarding the experiments of Fig. 3. First, absolute XMCD asymmetry values are lower for the LSMO (001) surface [Fig. 3(c)] than the LSMO (011) surface [Fig. 3(d)]. This discrepancy is probably due to reduced magnetization [43] and altered Mn valence [44] within the approximately 7-nm electron escape depth of PEEM, and it is consistent with the small difference in bulk saturation magnetization [45] [Figs. 1(a) and 1(b)]. Second, imperfect lithography significantly rounds the corners of our LSMO (011) dots, but single-domain switching is nevertheless achieved. Therefore, this rounding may be ignored here, as it has no qualitative influence on the switching process that we describe. (The rounding is, however, liable to modify the switching field if it increases the demagnetizing field at a given nucleation site [9–11].)

C. Magnetization reversal in electrodes

Variable-width LSMO (001) electrodes of length 30 μm behave just like the corresponding dots [Fig. 3(c)], as similar experiments reveal that magnetization reversal proceeds via multidomain states of magnetization [Figs. 4(a) and 4(b)]. From these images, we find that the switched fraction shows

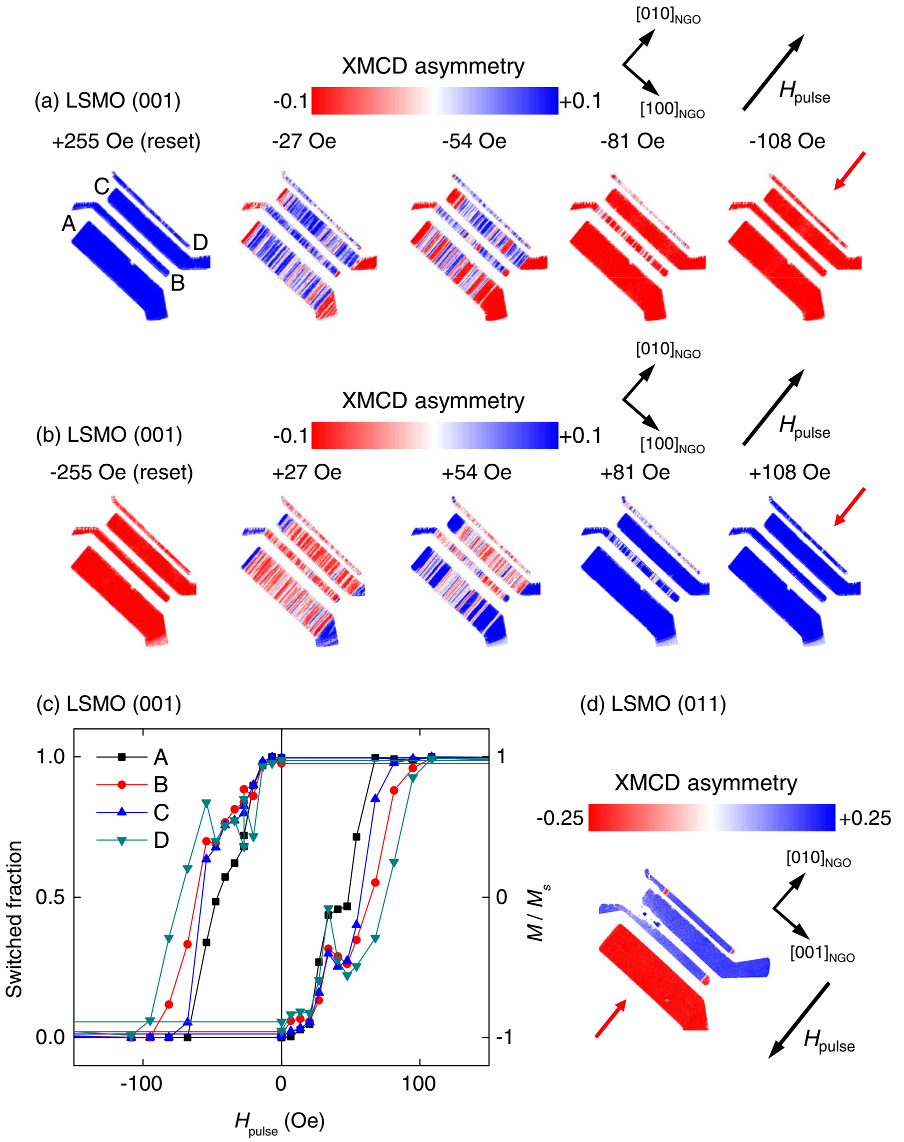

FIG. 4. Visualization of magnetization reversal in LSMO electrodes at 150 K. (a),(b) Selected zero-field XMCD-PEEM images of LSMO (001) electrodes A–D after applying easy-axis fields H_{pulse} as indicated. (c) The corresponding fraction of switched domains in electrodes A–D at remanence versus the last field applied H_{pulse} (data from tracks running off at some angle to remote contact pads are excluded). (d) Zero-field XMCD-PEEM image of LSMO (011) electrodes A–D obtained during a minor loop in which field H_{pulse} is applied in the direction indicated. XMCD asymmetry represents projection of in-plane surface magnetization onto in-plane projection of grazing-incidence beam direction (red arrows). For (a),(b), darkest red contrast depicts magnetization pointing top right; darkest blue contrast depicts magnetization pointing bottom left. For (c), the reverse holds true as in-plane projection of beam is reversed. We obtain all data after zero-field cooling. The main rectangular regions of electrodes A–D are 30 μm long, and their widths are 10, 3, 6, and 2 μm, respectively.

a hysteretic dependence on H_{pulse} [Fig. 4(c)]. This hysteresis mimics the major-loop hysteresis observed in unpatterned LSMO (001) [Fig. 2(a)], with minor differences attributed to shape anisotropy, edge roughness, and imaging at remanence. We find that reverse domains are created in all four electrodes at $|H_{\mathrm{pulse}}| \lesssim 20$ Oe, and we find evidence for an inverse correlation between electrode width and switching field that may indicate a propensity for Zeeman-driven domain switching to dominate edge pinning in wide electrodes. Although these electrodes do not support an AP magnetic configuration at remanence, we see for $H_{\mathrm{pulse}} = -68$ Oe that 95% of the domains in electrode *C* are AP with respect to 60% of the domains in electrode *D* [Fig. 4(c)]. By contrast, for similar electrodes of LSMO (011), we observe an AP configuration at remanence during a minor loop [Fig. 4(d)], as expected given the behavior of the corresponding dots [Fig. 3(d)]. (Arcing during PEEM caused damage visible top left and precluded the collection of data as a function of H_{pulse}.)

D. Micromagnetic simulation of patterned elements

The sharp switching in our unpatterned [Fig. 2(b)] and patterned [Figs. 3(d) and 4(d)] films of LSMO (011) arises via the free propagation of DWs after nucleating reverse domains by overcoming an energy barrier. This energy barrier to nucleation arises from large anisotropy [Fig. 1(g)] according to a simple analytical model [2]. Following magnetic saturation, nucleation at a given site requires the application of a reverse field if the effective anisotropy K_{eff} exceeds some threshold value such that

$$K_{\mathrm{eff}} > \frac{\mu_0 N_d M_s^2}{2}, \qquad (2)$$

where N_d is the local demagnetizing factor, and M_s is saturation magnetization. (By contrast, if K_{eff} does not exceed the threshold value, then domains will form before reaching zero field.) It is challenging to estimate N_d and K_{eff} because both are local properties of the nucleation site

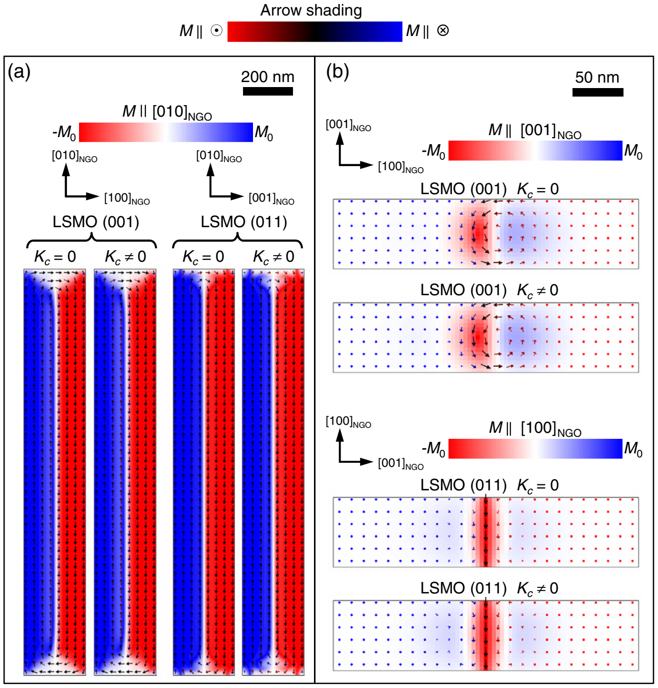

FIG. 5. Simulations of domain walls in patterned LSMO films. Simulated $300 \times 2000\ \mathrm{nm}^2$ slabs of height 68 nm, with and without out-of-plane film anisotropy K_c [$3\ \mathrm{kJ\,m^{-3}}$ for LSMO (001), $10\ \mathrm{kJ\,m^{-3}}$ for LSMO (011)]. (a) Horizontal cross sections at height 34 nm. (b) Vertical domain-wall cross sections near slab centers. The magnetocrystalline easy axis is along the long axis of each LSMO strip, in contrast with our experiments on electrodes, in order to simulate the intrinsic behavior of long DWs. Arrows indicate direction of magnetization component in plane of page; shading indicates magnitude of magnetization component along page vertical. Arrow shading indicates magnitude of magnetization component perpendicular to the viewing plane.

and because K_{eff} is a function of both magnetocrystalline and shape anisotropy. Therefore, we perform simulations, as described below, in order to explore the existence of nucleation barriers.

In order to investigate the link between magnetic anisotropy and micromagnetic structure in our patterned films of LSMO (001) and LSMO (011) at 150 K, we perform micromagnetic simulations of DWs in zero applied field (Fig. 5) and quasistatic magnetic switching (Fig. 6). The zero-field DWs are simulated in rectangular LSMO slabs containing a single DW (Fig. 5) (see Sec. II). These slabs for DW simulations are elongated parallel to their easy axes in order to minimize the effect of poles and do not correspond to the spintronic electrodes of Fig. 4 which are elongated perpendicular to their easy axes. Substrate orientation is parametrized using the in-plane anisotropy constants K_1 and K_a deduced earlier, and we investigate the effect of introducing a uniaxial out-of-plane anisotropy $K_c > 0$. Given that we cannot measure K_c because of the large out-of-plane demagnetizing factor combined with strong substrate paramagnetism, we assume for each substrate orientation a value comparable in magnitude with K_1 and K_a (Table I). For simplicity, we neglect the small influence of strain on magnetization and exchange stiffness [46,47], and we neglect the influence of inhomogeneous strain associated with edges, defects, and structural domains [41,42].

Assuming an initial state in which a through-thickness vertical Bloch wall bisects each LSMO slab, relaxation to an energy minimum yields small closure domains for both substrate orientations, with and without the additional anisotropy K_c [Fig. 5(a)]. (Alternative initial states result in essentially the same magnetic structure, but in some cases, there are Bloch lines [48] between wall segments of opposite chirality.) Cross-sectional slab views [Fig. 5(b)] reveal that DW structures depend strongly on the in-plane anisotropies K_1 and K_a associated with LSMO film orientation but only weakly on out-of-plane anisotropy K_c, consistent with literature simulations [49] where $K_1 = K_c = 0$. For LSMO (001), the DWs are relatively wide ($W \sim 90$ nm) and possess a vortexlike asymmetric Bloch wall structure [49–51] with little stray field. For LSMO (011), narrower DWs ($W \sim 40$ nm) possess a symmetric Bloch wall structure [49], and all moments in the DW lie out of plane, resulting in a stray field.

Both types of DWs differ from a simple Bloch wall, whose energy is 2–3 times larger. (For an LSMO film of the same thickness $t = 68$ nm, a simple Bloch wall has energy per unit length $4t\sqrt{AK_{\mathrm{eff}}} = 144\ \mathrm{pJ\,m^{-1}}$, where effective anisotropy $K_{\mathrm{eff}} = \frac{1}{2}\mu_0 M_s^2$. As for the simulations, we use saturation magnetization $M_s = 460\ \mathrm{kA\,m^{-1}}$ and exchange stiffness $A = 2.1 \times 10^{-12}\ \mathrm{J\,m^{-1}}$. Both are calculated as described in Sec. II and are consistent with Ref. [19].) The DW energy is slightly higher for LSMO (011) than LSMO (001) (Table I), because more surface poles produce more stray and demagnetizing fields and because the narrower DW structure results in a higher exchange energy. Counterintuitively, the DW anisotropy energy itself is rather insensitive to the magnitude of the in-plane anisotropy, as the large in-plane anisotropy of LSMO (011) forces the magnetization of the narrow DW to lie out of plane [Fig. 5(b)]. The higher DW energy in LSMO (011) that we calculate here should disfavor domain nucleation, consistent with the nucleation-limited switching discussed above.

In order to gain more insight into the magnetization reversal observed experimentally at remanence, we simulate $1 \times 1\ \mu\mathrm{m}^2$ LSMO dots in an easy-axis magnetic field H that is quasistatically cycled in ±250 Oe (dot size ≫ DW width is sufficient for qualitative comparison with the $5 \times 5\ \mu\mathrm{m}^2$ dots of Fig. 3). We distinguish the two substrate orientations by varying the anisotropy from low [LSMO (001)] to high [LSMO (011)] (Fig. 6). We set $K_c = 0$ given that K_c has little influence on domain energetics (Table I). We neglect the slightly higher saturation magnetization of LSMO (011)

TABLE I. Anisotropy constants and energies for DWs in LSMO films on NGO substrates. K_1 and K_a of Eq. (1) are obtained from magnetometry (Fig. 1) and we assume similar order-of-magnitude values for out-of-plane anisotropy $K_c \neq 0$. DW energies are normalized by DW length not area, as vertical and horizontal projections of DW cross-sectional area are comparable.

	Anisotropy ($\mathrm{kJ\,m^{-3}}$)			Energy ($\mathrm{pJ\,m^{-1}}$)			
Sample	K_1	K_a	K_c	Exchange	Stray + demag field	Anisotropy	Total
LSMO (001)	−2.3	6.5	0	38	2	9	49
LSMO (001)	−2.3	6.5	3	39	2	5	46
LSMO (011)	−13.4	34.2	0	46	12	8	66
LSMO (011)	−13.4	34.2	10	43	14	−2	55

[Figs. 1(a) and 2(b)] and the larger difference in surface magnetization [Figs. 3(c) and 3(d)]. This is reasonable given that a larger magnetization implies a larger demagnetization energy and, therefore, a larger tendency for domains to form, while both our experiments [Figs. 3(c) and 3(d)] and simulations (Fig. 6) show that domains form readily in LSMO (001) and not LSMO (011). We also neglect relaxation of the small strain at film edges

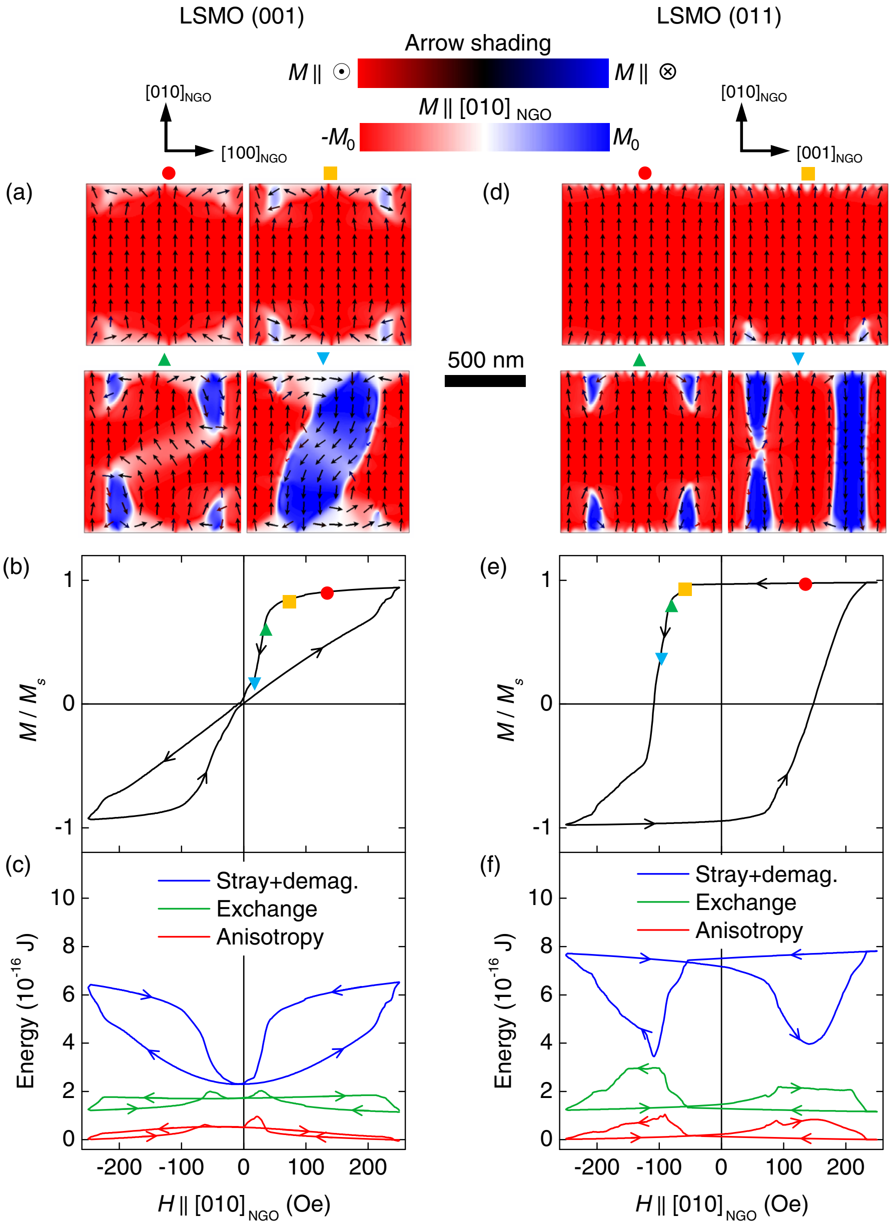

FIG. 6. Simulations of magnetization reversal in patterned LSMO films. Simulated $1000 \times 1000\ \mathrm{nm}^2$ slabs of height 68 nm, for (a)–(c) LSMO (001) and (d)–(f) LSMO (011), with out-of-plane anisotropy $K_c = 0$. (a),(d) Horizontal cross sections at height 34 nm, showing early stages of magnetization reversal at fields indicated by colored symbols that appear in (b),(e). Arrows indicate direction of magnetization component in the plane of the page; shading indicates magnitude of magnetization component along page vertical. Arrow shading indicates magnitude of magnetization component perpendicular to the viewing plane. (b),(e) Plots of normalized magnetization M versus applied field H (M_s is saturation magnetization). (c),(f) The corresponding variations of stray and demagnetizing field energy, exchange energy, and anisotropy energy (arbitrary vertical offset introduced for clarity, Zeeman energy $-\mu_0 MH$ omitted for clarity).

where reverse domains nucleate (this 0.16% strain lies perpendicular to the magnetic easy axis for both substrate orientations [30]). Last, we neglect the existence of pinning centers, which is reasonable here, as pinning does not influence the ability of our simulations to discriminate whether the onset of switching requires field reduction or field reversal.

For the LSMO (001) dot with relatively weak uniaxial anisotropy, reducing H from 250 Oe initially produces canting and nascent flux-closure structures near each pole [red circle, Fig. 6(a)]. Further reducing H towards zero almost completely demagnetizes the dot via the development of reverse domains that nucleate from the flux-closure pattern [Figs. 6(a) and 6(b)]. By contrast, demagnetization in our experiments requires a reverse field H_p [Fig. 2(a)] to unpin DWs from imperfections that we do not simulate. Our simulations show that the demagnetization process occurs because the reduction of stray and demagnetizing field energy exceeds the combined increase in anisotropy energy and exchange energy [Fig. 6(c)].

For the LSMO (011) dot with relatively strong uniaxial anisotropy, reducing H from 250 Oe initially has little effect on magnetic structure [red circle, Fig. 6(d)]. Further reducing H through zero nucleates reverse domains in the canted polar regions while dot magnetization remains high [yellow square, Figs. 6(d) and 6(e)]. The nucleation field is smaller in our experiments due to thermal activation and edge roughness [$|H_n| \sim 20$ Oe, Fig. 2(b)]. Unlike the LSMO (001) dot, the combined increase in anisotropy energy and exchange energy during domain-wall nucleation exceeds the reduction of stray and demagnetizing field energy [Fig. 6(f)], inhibiting demagnetization until $|H|$ is so large that Zeeman energy $-\mu_0 MH$ drives magnetization reversal.

Our simulations, therefore, show that magnetic anisotropy strength alone is sufficient to discriminate between the experimentally observed magnetization reversal in LSMO (011) and LSMO (001).

E. Predicted spintronic performance

We now exploit the above study of magnetic switching in order to predict the performance of lateral spin valves in which we imagine our LSMO electrodes to be connected by nonmagnetic channels. We assume that no spin relaxation occurs in the channel and that interfacial resistance dominates two-terminal device resistance. In practice, suitable channel materials will include carbon nanotubes [16] and graphene [52].

For homogeneously magnetized LSMO (011) electrodes [Fig. 4(d)], device resistance may be described by reducing the drift-diffusion model for spin transport [53,54] to four resistors that represent the two transport spin states at the two interfaces. Assuming that these interfaces have equal area, device resistance in the P and AP configurations (R_P and R_AP) will then differ, as described via the following simple expression for magnetoresistance $\mathrm{MR} = (R_\mathrm{AP} - R_\mathrm{P})/R_\mathrm{P} = \gamma^2/(1-\gamma^2)$, i.e., an expression that represents half the MR for a magnetic tunnel junction [11] (γ is the interfacial spin polarization for LSMO).

For partially switched LSMO (001) electrodes [Figs. 4(a)–4(c)], the spin-up and spin-down transport electrons experience an interfacial resistance that depends on the orientation of the interfacial electrode magnetization, necessitating an eight-resistor model [Fig. 7(a)]. The resistance of this device is predicted to be

$$R(f_1, f_2) = \left[\begin{array}{c} \left[\left(\frac{f_1 A_1}{r_+} + \frac{(1-f_1)A_1}{r_-}\right)^{-1} + \left(\frac{f_2 A_2}{r_+} + \frac{(1-f_2)A_2}{r_-}\right)^{-1}\right]^{-1} \\ + \\ \left[\left(\frac{(1-f_1)A_1}{r_+} + \frac{f_1 A_1}{r_-}\right)^{-1} + \left(\frac{(1-f_2)A_2}{r_+} + \frac{f_2 A_2}{r_-}\right)^{-1}\right]^{-1} \end{array}\right]^{-1}, \tag{3}$$

where $r_\pm = 2r_b^*(1 \mp \gamma)$ is the interfacial resistance-area product [53,54] for transport spins parallel (antiparallel) to the local electrode magnetization such that $+$ and $-$ denote majority and minority carriers, respectively (r_b^* is the spin-averaged resistance). Interface i occupies area $A_i (i = 1, 2)$, and fraction f_i [fraction $(f_i - 1)$] of the underlying domains is magnetized in the spin-up [spin-down] direction.

For $\gamma = 0.5$, values of (f_1, f_2) for adjacent electrode pairs of area (A_1, A_2) obtained from the remanent-field-dependent XMCD-PEEM data [Figs. 4(a)–4(c)] are used to compute remanent magnetoresistance $\mathrm{RMR} = \Delta R/R_\mathrm{P} = [R(f_1, f_2) - R(0,0)]/R(0,0)$ for gradual switching [solid lines, Fig. 7(b)]. The peak values are more than 3 times less than the corresponding RMR values for the fully AP configurations [dashed lines, Fig. 7(b)] in LSMO (011) with sharp switching [Fig. 4(d)]. This underlines how complete switching between fully P and AP states is important for both large signals and accurate determination of spintronic parameters.

Increasing γ towards the more realistic value [14] of 0.95 causes a stark divergence between the maximum RMR values during gradual switching ($\mathrm{RMR}_\mathrm{peak}$) and complete switching (RMR_AP), i.e., a fall in RMR efficiency $\eta = \mathrm{RMR}_\mathrm{peak}/\mathrm{RMR}_\mathrm{AP}$ [Fig. 7(c)]. Therefore, knowledge of magnetic switching is particularly important in spintronic devices with little spin relaxation and highly spin-polarized electrodes, i.e., precisely the conditions sought for large-spin signals. Thus, as material and interface properties are improved, the electrode-switching variable can become only more critical.

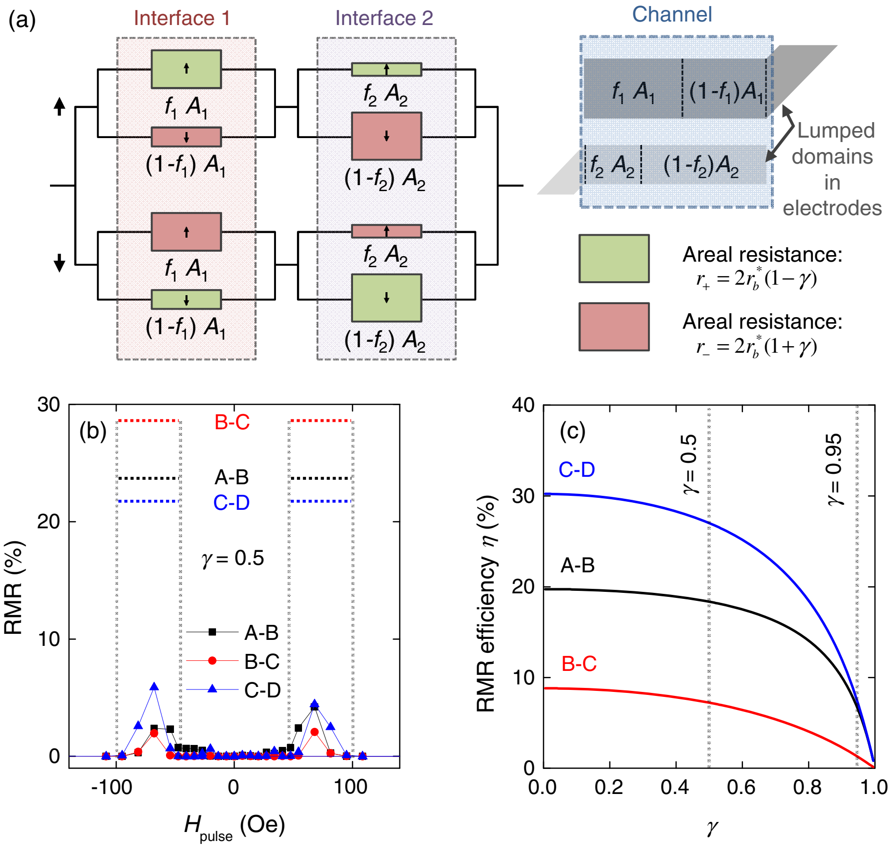

FIG. 7. Predictions of remanent MR for LSMO electrodes on NGO (001). (a) Eight-resistor model for a nonmagnetic conducting channel with no spin relaxation spanning two electrodes in which domains preclude a fully AP configuration. Heavy arrows indicate incoming transport spins at left, light arrows indicate domain magnetizations, and the effective area of each resistor is stated. The low (high) areal resistance for majority (minority) electrons tunneling through each interface is represented by green (red) shading. Interface i occupies area A_i ($i = 1, 2$), and fraction f_i [fraction $(1 - f_i)$] of the underlying domains are magnetized up [down] with respect to a direction we choose by convention. Inset, top right: Schematic indicates these areal fractions by lumping domains in the two electrodes (gray) that are spanned by the channel (blue). (b) For interfacial spin polarization $\gamma = 0.5$, we plot RMR(H_{pulse}) (symbols) for adjacent electrode pairs that undergo the gradual switching of Figs. 4(a)–4(c). For comparison, we plot the expected RMR for electrodes that undergo sharp and complete switching (dotted lines). (c) RMR efficiency η versus γ for the same electrode pairs. Dotted lines represent the values $\gamma = 0.5$ and $\gamma = 0.95$ discussed in the text.

V. CONCLUSIONS

In summary, we demonstrate how NGO substrate orientation controls magnetic anisotropy and, therefore, magnetic switching in patterned elements of epitaxial thin-film LSMO. Our imaging study shows that films in the (001) orientation on NGO (001) exhibit gradual switching via the creation and depinning of many small domains. This gradual switching is desirable for memristors or artificial neurons [7,8], but it compromises the performance of binary spintronic devices. For example, if the assumption that spin valves develop fully P and AP states is not correct, as one may suspect from gradual electrical switching [5,6], then the resulting MR will be suppressed, and this leads to underestimates of electrode spin polarization and channel spin-diffusion length. This problem may be widespread given that binary spintronic devices are not normally subjected to magnetic imaging.

In the future, we hope that the approach presented here will benefit performance and analysis of various spintronic devices fabricated from various electrode materials. Controlling the switching process by tailoring global anisotropy, as we do here, can also be achieved via control of film thickness, chemical composition, or microstructural disorder. Alternatively, one may locally tailor magnetic anisotropy by area-selective etching, deoxygenation via Joule heating, or ion implantation. This latter strategy will immediately render mandatory the magnetic imaging that we argue to be necessary in general.

ACKNOWLEDGMENTS

This work is funded by Grant No. F/09 154/E from The Leverhulme Trust and a UK EPSRC DTA grant (L. C. P.), Isaac Newton Trust Grant No. 10.26(u) and UK EPSRC Grant No. EP/E0026206 (M. G.), and Herchel Smith and Spanish MEC Ramón y Cajal Fellowships (X. M.). The authors are grateful to A. Jenkins for useful discussions.

---

[1] I. Žutić, J. Fabian, and S. Das Sarma, Spintronics: Fundamentals and applications, Rev. Mod. Phys. **76**, 323 (2004).

[2] B. D. Cullity and C. D. Graham, *Introduction to Magnetic Materials*, 2nd ed. (Wiley, Hoboken, NJ, USA, 2009).

[3] W. Wernsdorfer, C. Thirion, N. Demoncy, H. Pascard, and D. Mailly, Magnetisation reversal by uniform rotation (Stoner-Wohlfarth model) in FCC cobalt nanoparticles, J. Magn. Magn. Mater. **242–245**, 132 (2002).

[4] D. Givord, M. Rossignol, and V. M. T. S. Barthem, The physics of coercivity, J. Magn. Magn. Mater. **258–259**, 1 (2003).

[5] K. Tsukagoshi, B. W. Alphenaar, and H. Ago, Coherent transport of electron spin in a ferromagnetically contacted carbon nanotube, Nature (London) **401**, 572 (1999).

[6] B. Dlubak, M.-B. Martin, C. Deranlot, B. Servet, S. Xavier, R. Mattana, M. Sprinkle, C. Berger, W. A. de Heer, F. Petroff, A. Anane, P. Seneor, and A. Fert, Highly efficient spin transport in epitaxial graphene on SiC, Nat. Phys. **8**, 557 (2012).

[7] X. Wang, Y. Chen, H. Xi, H. Li, and D. Dimitrov, Spintronic memristor through spin-torque-induced magnetization motion, IEEE Electron Device Lett. **30**, 294 (2009).

[8] A. Chanthbouala, R. Matsumoto, J. Grollier, V. Cros, A. Anane, A. Fert, A. V. Khvalkovskiy, K. A. Zvezdin, K. Nishimura, Y. Nagamine, H. Maehara, K. Tsunekawa, A. Fukushima, and S. Yuasa, Vertical-current-induced domain-wall motion in MgO-based magnetic tunnel junctions with low current densities, Nat. Phys. **7**, 626 (2011).

[9] K. J. Kirk, J. N. Chapman, and C. D. W. Wilkinson, Switching fields and magnetostatic interactions of thin film magnetic nanoelements, Appl. Phys. Lett. **71**, 539 (1997).

[10] T. Schrefl, J. Fidler, K. J. Kirk, and J. N. Chapman, Domain structures and switching mechanisms in patterned magnetic elements, J. Magn. Magn. Mater. **175**, 193 (1997).

[11] M. Herrmann, S. McVitie, and J. N. Chapman, Investigation of the influence of edge structure on the micromagnetic behavior of small magnetic elements, J. Appl. Phys. **87**, 2994 (2000).

[12] J.-H. Park, E. Vescovo, H.-J. Kim, C. Kwon, R. Ramesh, and T. Vankatesan, Direct evidence for a half-metallic ferromagnet, Nature (London) **392**, 794 (1998).

[13] J. Z. Sun, W. J. Gallagher, P. R. Duncombe, L. Krusin-Elbaum, R. A. Altman, A. Gupta, Y. Lu, G. Q. Gong, and G. Xiao, Observation of large low-field magnetoresistance in trilayer perpendicular transport devices made using doped manganate perovskites, Appl. Phys. Lett. **69**, 3266 (1996).

[14] M. Bowen, M. Bibes, A. Barthélémy, J.-P. Contour, A. Anane, Y. Lemaître, and A. Fert, Nearly total spin polarization in $La_{2/3}Sr_{1/3}MnO_3$ from tunneling experiments, Appl. Phys. Lett. **82**, 233 (2003).

[15] Z. H. Xiong, D. Wu, Z. Valy Vardeny, and J. Shi, Giant magnetoresistance in organic spin-valves, Nature (London) **427**, 821 (2004).

[16] L. E. Hueso, J. M. Pruneda, V. Ferrari, G. Burnell, J. P. Valdés-Herrera, B. D. Simons, P. B. Littlewood, E. Artacho, A. Fert, and N. D. Mathur, Transformation of spin information into large electrical signals using carbon nanotubes, Nature (London) **445**, 410 (2007).

[17] Y.-A. Soh, G. Aeppli, N. D. Mathur, and M. G. Blamire, Temperature dependent phenomena in $La_{1-x}Sr_xMnO_3$ films studied by magnetic force microscopy, J. Appl. Phys. **87**, 6743 (2000).

[18] M. E. Hawley, G. W. Brown, P. C. Yashar, and C. Kwon, H-dependent magnetic domain structures in $La_{0.67}Sr_{0.33}MnO_3$ thin films, J. Cryst. Growth **211**, 86 (2000).

[19] R. Akiyama, H. Tanaka, T. Matsumoto, and T. Kawai, Spin-polarized scanning tunneling microscopy on half-metallic manganite thin film with half-metallic manganite tip, Appl. Phys. Lett. **79**, 4378 (2001).

[20] T. Taniuchi, H. Kumigashira, M. Oshima, T. Wakita, T. Yokoya, M. Kubota, K. Ono, H. Akinaga, M. Lippmaa, M. Kawasaki, and H. Koinuma, Observation of step-induced magnetic domain formation in $La_{1-x}Sr_xMnO_3$ thin films by photoelectron emission microscopy, Appl. Phys. Lett. **89**, 112505 (2006).

[21] E. P. Houwman, G. Maris, G. M. De Luca, N. Niermann, G. Rijnders, D. H. A. Blank, and S. Speller, Out-of-plane magnetic domain structure in a thin film of $La_{0.67}Sr_{0.33}MnO_3$ on $SrTiO_3$ (001) observed by magnetic force microscopy, Phys. Rev. B **77**, 184412 (2008).

[22] P. Lecoeur, P. L. Trouilloud, G. Xiao, A. Gupta, G. Q. Gong, and X. W. Li, Magnetic domain structures of $La_{0.67}Sr_{0.33}MnO_3$ thin films with different morphologies, J. Appl. Phys. **82**, 3934 (1997).

[23] L. S. Uspenskaya, T. Nurgaliev, and S. Miteva, Magnetization reversal of thin $La_{0.7}Sr_{0.3}MnO_3$ manganite films grown on $LaAlO_3$, J. Phys. D **42**, 185006 (2009).

[24] Y. Takamura, R. V. Chopdekar, A. Scholl, A. Doran, J. A. Liddle, B. Harteneck, and Y. Suzuki, Tuning magnetic domain structure in nanoscale $La_{0.7}Sr_{0.3}MnO_3$ islands, Nano Lett. **6**, 1287 (2006).

[25] E. J. Kim, J. L. R. Watts, B. Harteneck, A. Scholl, A. Young, A. Doran, and Y. Suzuki, Magnetic domain structure of $La_{0.7}Sr_{0.3}MnO_3$ nanoislands: Experiment and simulation, J. Appl. Phys. **109**, 07D712 (2011).

[26] P. Perna, L. Méchin, M. Saïb, J. Camarero, and S. Flament, Imaging the magnetization reversal of step-induced uniaxial magnetic anisotropy in vicinal epitaxial $La_{0.7}Sr_{0.3}MnO_3$ films, New J. Phys. **12**, 103033 (2010).

[27] Y. Konishi, Z. Fang, M. Izumi, T. Manako, M. Kasai, H. Kuwahara, M. Kawasaki, K. Terakura, and Y. Tokura, Orbital-state-mediated phase-control of manganites, J. Phys. Soc. Jpn. **68**, 3790 (1999).

[28] C. Kwon, M. C. Robson, K.-C. Kim, J. Y. Gu, S. E. Lofland, S. M. Bhagat, Z. Trajanovic, M. Rajeswari, T. Venkatesan, A. R. Kratz, R. D. Gomez, and R. Ramesh, Stress-induced effects in epitaxial $(La_{0.7}Sr_{0.3})MnO_3$ films, J. Magn. Magn. Mater. **172**, 229 (1997).

[29] L. C. Phillips, M. Ghidini, X. Moya, F. Maccherozzi, S. S. Dhesi, and N. D. Mathur, Low-temperature transverse magnetic domains in nominally uniaxial $La_{0.67}Sr_{0.33}MnO_3$ films on $NdGaO_3$ (001), J. Phys. D **46**, 032002 (2013).

[30] H. Boschker, M. Mathews, E. P. Houwman, H. Nishikawa, A. Vailionis, G. Koster, G. Rijnders, and D. H. A. Blank, Strong uniaxial in-plane magnetic anisotropy of (001)- and (011)-oriented $La_{0.67}Sr_{0.33}MnO_3$ thin films on $NdGaO_3$ substrates, Phys. Rev. B **79**, 214425 (2009).

[31] R. Bertacco, S. Brivio, M. Cantoni, A. Cattoni, D. Petti, M. Finazzi, F. Ciccacci, A. A. Sidorenko, M. Ghidini, G. Allodi, and R. De Renzi, Proximity effects induced by a gold layer on $La_{0.67}Sr_{0.33}MnO_3$ thin films, Appl. Phys. Lett. **91**, 102506 (2007).

[32] https://www.repository.cam.ac.uk/handle/1810/251379.

[33] C. Kittel, *Introduction to Solid State Physics*, 5th ed. (Wiley, New York, 1976).

[34] U. Atxitia, D. Hinzke, O. Chubykalo-Fesenko, U. Nowak, H. Kachkachi, O. N. Mryasov, R. F. Evans, and R. W. Chantrell, Multiscale modeling of magnetic materials: Temperature dependence of the exchange stiffness, Phys. Rev. B **82**, 134440 (2010).

[35] M. J. Donahue and D. G. Porter, *OOMMF User's Guide*, Version 1.0 NISTIR 6376 (National Institute of Standards and Technology, Gaithersburg, MD, 1999).

[36] See the Supplemental Material at http://link.aps.org/supplemental/10.1103/PhysRevApplied.4.064004 for x-ray diffraction evidence of coherent strain in our LSMO films.

[37] M. Mathews, E. P. Houwman, H. Boschker, G. Rijnders, and D. H. A. Blank, Magnetization reversal mechanism in $La_{0.67}Sr_{0.33}MnO_3$ thin films on $NdGaO_3$ substrates, J. Appl. Phys. **107**, 013904 (2010).

[38] W. Yan, Ph.D. thesis, University of Cambridge, 2014.

[39] R. Skomski, *Simple Models of Magnetism* (Oxford University Press, Oxford, 2008).

[40] K.-D. Durst and H. Kronmüller, The coercive field of sintered and melt-spun NdFeB magnets, J. Magn. Magn. Mater. **68**, 63 (1987).

[41] N. Farag, M. Bobeth, W. Pompe, A. E. Romanov, and J. S. Speck, Modeling of twinning in epitaxial (001)-oriented $La_{0.67}Sr_{0.33}MnO_3$ thin films, J. Appl. Phys. **97**, 113516 (2005).

[42] U. Gebhardt, N. V. Kasper, A. Vigliante, P. Wochner, H. Dosch, F. S. Razavi, and H.-U. Habermeier, Formation and Thickness Evolution of Periodic Twin Domains in Manganite Films Grown on $SrTiO_3(001)$ Substrates, Phys. Rev. Lett. **98**, 096101 (2007).

[43] J.-H. Park, E. Vescovo, H.-J. Kim, C. Kwon, R. Ramesh, and T. Venkatesan, Magnetic Properties at Surface Boundary of a Half-Metallic Ferromagnet $La_{0.7}Sr_{0.3}MnO_3$, Phys. Rev. Lett. **81**, 1953 (1998).

[44] M. P. de Jong, I. Bergenti, V. A. Dediu, M. Fahlman, M. Marsi, and C. Taliani, Evidence for Mn^{2+} ions at surfaces of $La_{0.7}Sr_{0.3}MnO_3$ thin films, Phys. Rev. B **71**, 014434 (2005).

[45] R. V. Chopdekar, E. Arenholz, and Y. Suzuki, Orientation and thickness dependence of magnetization at the interfaces of highly spin-polarized manganite thin films, Phys. Rev. B **79**, 104417 (2009).

[46] A. J. Millis, T. Darling, and A. Migliori, Quantifying strain dependence in "colossal" magnetoresistance manganites, J. Appl. Phys. **83**, 1588 (1998).

[47] C. Adamo, X. Ke, H. Q. Wang, H. L. Xin, T. Heeg, M. E. Hawley, W. Zander, J. Schubert, P. Schiffer, D. A. Muller, L. Maritato, and D. G. Schlom, Effect of biaxial strain on the electrical and magnetic properties of (001) $La_{0.7}Sr_{0.3}MnO_3$ thin films, Appl. Phys. Lett. **95**, 112504 (2009).

[48] A. Hubert and R. Schäfer, *Magnetic Domains* (Springer, Berlin, 1998), Sec. 3.6.5.

[49] K. Ramstöck, W. Hartung, and A. Hubert, The phase diagram of domain walls in narrow magnetic strips, Phys. Status Solidi (a) **155**, 505 (1996).

[50] A. E. LaBonte, Two-dimensional Bloch-type domain walls in ferromagnetic films, J. Appl. Phys. **40**, 2450 (1969).

[51] A. Hubert, Stray-field-free and related domain wall configurations in thin magnetic films (II), Phys. Status Solidi **38**, 699 (1970).

[52] D. Huertas-Hernando, F. Guinea, and A. Brataas, Spin-Orbit-Mediated Spin Relaxation in Graphene, Phys. Rev. Lett. **103**, 146801 (2009).

[53] T. Valet and A. Fert, Theory of the perpendicular magnetoresistance in magnetic multilayers, Phys. Rev. B **48**, 7099 (1993).

[54] A. Fert and H. Jaffrès, Conditions for efficient spin injection from a ferromagnetic metal into a semiconductor, Phys. Rev. B **64**, 184420 (2001).